Supporting Information

Boosting photoelectrochemical performance of BiVO$_4$ by borate

buffer activation: the role of trace iron impurities

Xiaohu CAO, Xuemeng Yu, Xihan Chen, Ruquan Ye*

Experiment section

Fabrication of BiVO$_4$ photoanodes

The BiVO$_4$ photoanodes were prepared according to the previous method[1]. First, a 0.04 M Bi(NO$_3$)$_3$ solution was prepared by dissolving Bi(NO$_3$)$_3$·5H$_2$O in 50 mL of the 0.4 M KI solution after its pH was adjusted to 1.7 by adding HNO$_3$. This solution was mixed with 20 mL of absolute ethanol containing 0.23 M p-benzoquinone. Then, the mixed solution was vigorously stirred for a few minutes. A typical three-electrode cell was used for electrodeposition BiOI. A FTO working electrode (WE), a Ag/AgCl reference electrode (RE), and a platinum counter electrode (CE) were used. Cathodic deposition was performed at -0.1 V vs. Ag/AgCl for 5 min. The dimethyl sulfoxide (DMSO) solution containing 0.2 M vanadyl acetylacetonate (VO(acac)$_2$) was dropped on the BiOI electrode. The piece was heated in a muffle furnace at 450 °C (ramping rate, 2 °C/min) for 2 h in air to convert BiOI to BiVO$_4$. Excess V$_2$O$_5$ present in the BiVO$_4$ electrodes was removed by soaking them in 1 M KOH solution for 15 min with gentle stirring. The resulting BiVO$_4$ electrodes were rinsed with DI water and dried at room temperature.

Synthesis of BiVO$_4$ powder

The BiVO$_4$ powder for annealing process was prepared by a typically hydrothermal procedure[2]. NH$_4$VO$_3$ (36 mmol) and Bi(NO$_3$)$_3$ (36 mmol) were dissolved in 300 mL of 2 M HNO$_3$. Then, the pH of the solution was adjusted to 2 with ammonia solution under stirring until orange precipitate formation. After ~2 h aging, it needed to pour some supernatant and transfer the precipitate to autoclaves for hydrothermally treatment (200

°C, 24 h). At last, the vivid yellow product was separated by filtration, washed with water for more than 3 times, and then dried at 60 °C.

Characterizations

The surface morphologies of the as-prepared electrodes were investigated by scanning electron microscope (SEM, Thermo Fisher, QUATTRO S) and transmission electron microscope (TEM, FEI Talos F200X). The crystalline structure of the samples was identified by X-ray diffraction analysis (XRD, Rigaku, Smartlab 9kw). UV-vis diffuse reflectance spectra were performed at Fourier transform infra-red spectrometer (Perkin Elmer Spectrum 100). X-ray photoelectron spectra (XPS, Thermo Scientific K-Alpha Nexsa) were measured Al Kα ray and calibrated with respect to the C 1s level of 284.8 eV. Inductively coupled plasma (ICP) atomic emission spectrometer (PE optima 6000) was used to detect the elements.

Photoelectrochemical measurements

The photoelectrochemical performance of photoanodes was operated on a CHI 650e workstation (CH Instruments Co.) with a three-electrode setup under simulated solar light irradiation (AM 1.5G filter, 100 mW/cm^2, Perfect Light). The fabricated electrode, Pt plate and Ag/AgCl electrode (3.5 M KCl) were used as working, counter and reference electrodes, respectively. Linear sweep voltammetry (LSV, 10 mV/s) and chronoamperometry (current-time curves, i-t) were mainly used for photocurrent density. Otherwise especially mentioned, a 1 M KBi borate buffer solution (pH 9.3) was used as electrolyte for all photoelectrochemical tests at ambient condition (~22 °C). All measured potentials were converted to V vs. RHE ($E_{RHE} = E_{Ag/AgCl} + 0.208 + 0.059 \times pH$). The soak activation was mostly immersion in buffer solutions for 12 hours under LED illumination. The spectrum of LED light (5W) is 380-840 nm at fixed distance 10 cm (around 0.3 Sun if detected by standard Si solar cell).

Applied bias photon-to-current efficiency (ABPE) was calculated from the LSV plots by following equation:

$$ABPE = \frac{I \times \left(1.23 - V_{bias}\right)}{P_{light}} \times 100\%$$

where I (mA/cm^2) is the measured photocurrent density from the LSV plots, V_{bias} (V vs.RHE) is the applied bias potential, P_{light} is the power density of incident illumination (100 mW/cm^2).

The photoelectrode efficiencies involve light absorption efficiency ($\eta_{absorption}$), charge separation efficiency ($\eta_{separation}$), and charge injection efficiency ($\eta_{injection}$) as by following equation:

$$\eta = \eta_{absorption} \times \eta_{separation} \times \eta_{injection}$$

With sodium sulfite (Na_2SO_3) as a hole scavenger, the charge injection efficiency ($\eta_{injection}$) can be determined as $J_{water}/J_{sodium\ sulfite}$ according to the typical LSV curves with/without 0.2 M Na_2SO_3 in the electrolyte. $\eta_{injection}$ was calculated using the equation as follow:

$$\eta_{injection} = \frac{J_{water}}{J_{sodium\ sulfite}} \times 100\%$$

the calculation of $\eta_{separation}$ was according to the following equation:

$$\eta_{separation} = \frac{J_{sodium\ sulfite}}{J_{abs}} \times 100\%$$

J_{abs} is mainly decided from light absorption results[3]. In our study, without any cocatalysts or heterogeneous semiconductors, and the light absorption of photoanodes before and after borate activation has trivial change. Finally, the J_{abs} can be considered almost unchanged.

Electrolyte purification

1 M KBi borate buffer solution (pH 9.3) was purified by a two-step electrolysis using two 100 mm × 100 mm × 0.05 mm high-purity Ti foil (99.99%) electrodes in a two-electrode setup[4]. The first electrolytic step was controlled at 2.5 V until the current decreased to 150 μA. Next, the constant current electrolysis step was conducted at 150 μA for at least 24 h (twice). During the electrolysis, the Ti foil electrodes were removed

from the solution before the electrolysis was terminated to avoid re-dissolution of electrodeposited impurities into the solution.
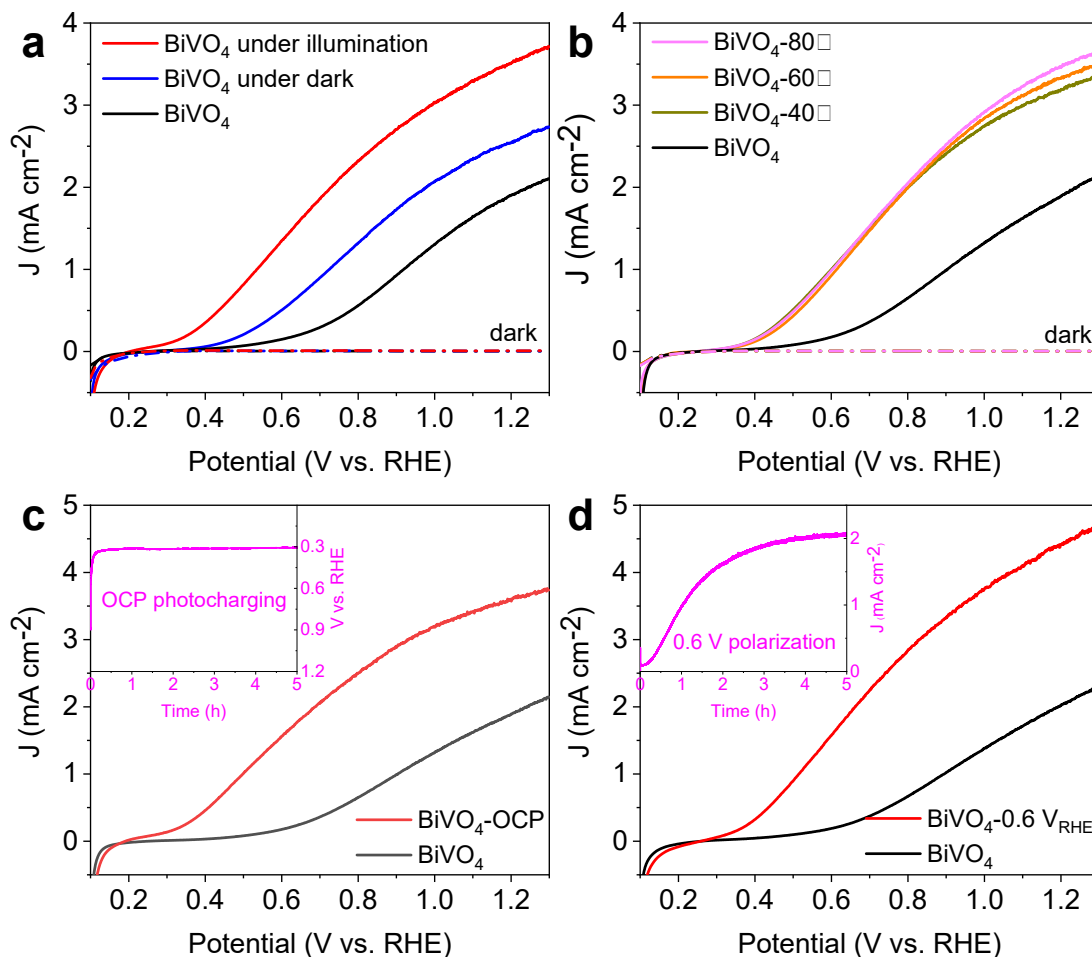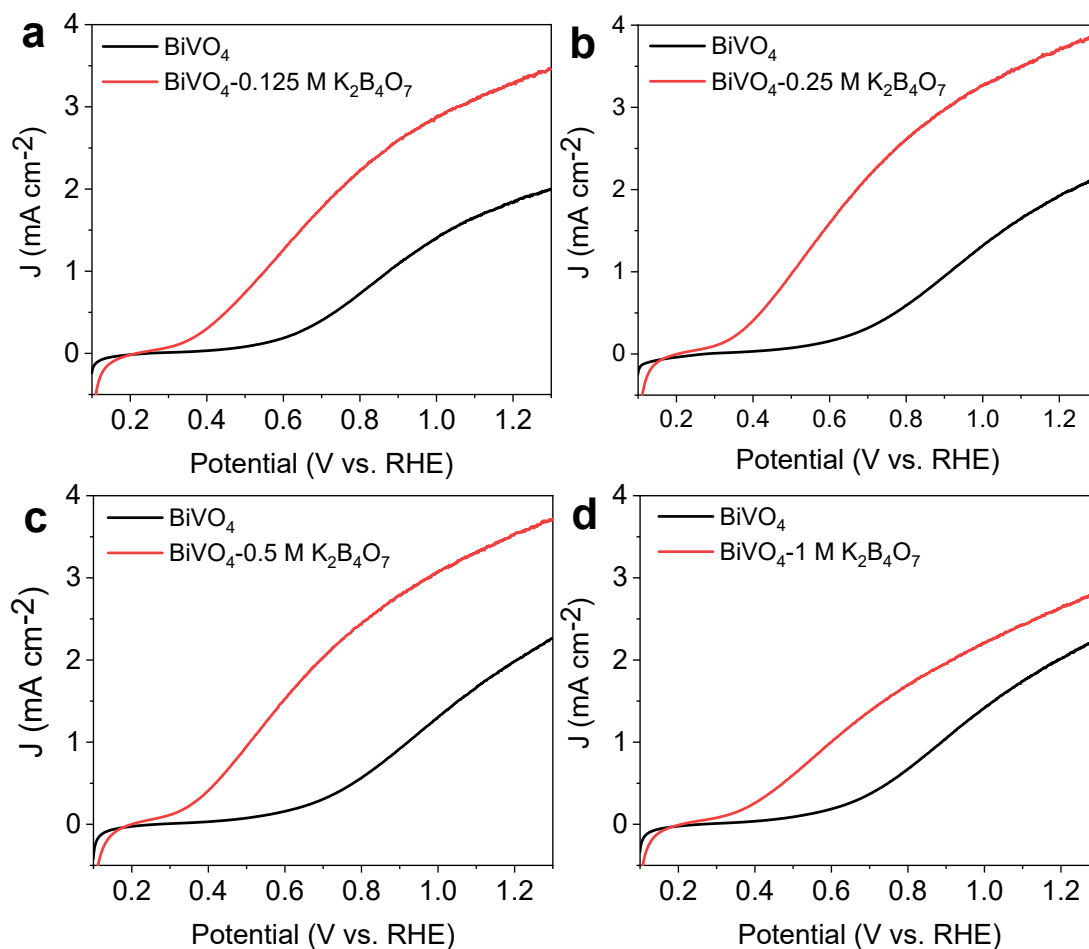

Figure S1. LSV curves of activated $BiVO_4$ and $BiVO_4$ photoanodes tested and soaked in (a) 0.01 M, (b) 0.1 M, (c) 0.5 M, (d) 1 M pH 9.3 KBi electrolyte solutions for 12 h under LED illumination.

First of all, the soaking treatment of $BiVO_4$ pieces was studied under dark and illumination conditions (Figure S1a). The $BiVO_4$ piece soaked in KBi buffer under dark already has an obvious improvement of photocurrent density from 2.0 mA/cm^2 to 2.6 mA/cm^2 at 1.23 V_{RHE}. Furthermore, the $BiVO_4$ piece soaked under illumination obtains higher photocurrent density of up to 3.6 mA/cm^2 and more negative onset potential than that under dark. This result implies that illumination can create a better condition for activating $BiVO_4$ by borate buffer. Furthermore, the role of temperature in activation

performance was also investigated under dark soaking conditions (Figure S1b). The BiVO$_4$ pieces were soaked in KBi buffer, maintaining temperatures at 40℃, 60℃ and 80℃. The results exhibit that mild heat can also help to activate the BiVO$_4$ electrode, achieving the photocurrent density of 3.2~3.5 mA/cm^2 at 1.23 V$_{RHE}$. In addition, open-circuit potential (OCP) photocharging treatment and photo-polarization treatment display even better activation performance as reported by papers with different explanations[5, 6]. From the linear scan voltammetry (LSV) curves of BiVO$_4$ photoanode with OCP photocharging treatment, the photocurrent density is enhanced to 3.7 mA/cm^2 at 1.23 V$_{RHE}$ with more negative onset potential (Figure S1c). For the photo-polarization treatment (Figure S1d), the BiVO$_4$ photoanode obtains the best activation photocurrent of 4.5 mA/cm^2 at 1.23 V$_{RHE}$.
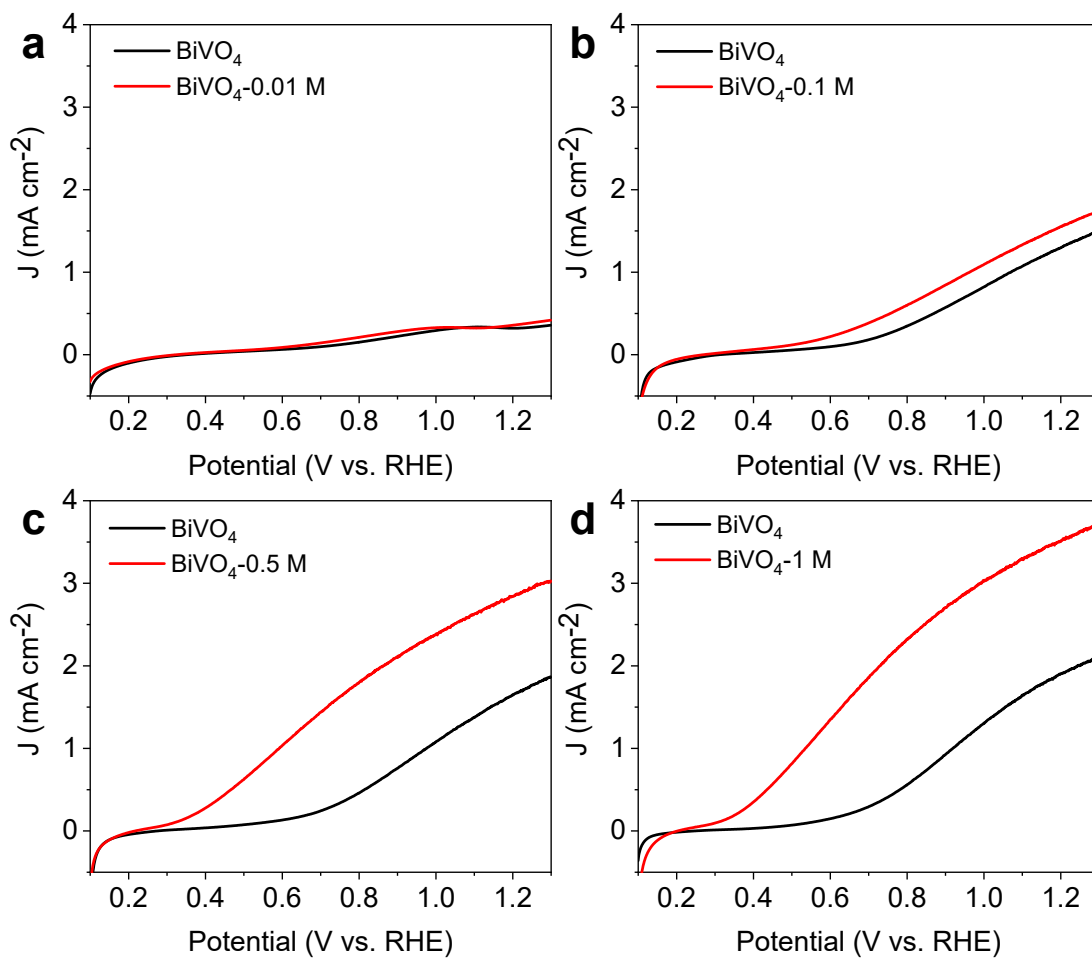
Figure S2. LSV curves of activated $BiVO_4$ and $BiVO_4$ photoanodes tested and soaked in (a) 0.01 M, (b) 0.1 M, (c) 0.5 M, (d) 1 M pH 9.3 KBi electrolyte solutions for 12 h under LED illumination.

Figure S3. LSV curves of activated $BiVO_4$ and $BiVO_4$ photoanodes tested and soaked in (a) 0.125 M, (b) 0.25 M, (c) 0.5 M, (d) 1 M $K_2B_4O_7$ electrolyte solutions for 12 h under LED illumination.

For investigating the relationship at higher concentrations, the $K_2B_4O_7$ is individually used to prepare the borate buffers considering the limited solubility of boric acid (H_3BO_3).

The borate concentrations of 0.125 M, 0.25 M, 0.5 M, 1 M $K_2B_4O_7$ solutions are 0.5 M, 1 M, 2 M, 4 M. The high concentration solution of $K_2B_4O_7$ was prepared by heating and then cooling to room temperature. The high concentration solution of $K_2B_4O_7$ is metastable solution and will recrystallize from solution after standing for several days. The pH values of 0.125 M, 0.25 M, 0.5 M, and 1 M $K_2B_4O_7$ electrolyte solutions are around 9.3, 9.4, 9.5, and 9.7, which are very close for activation treatment.
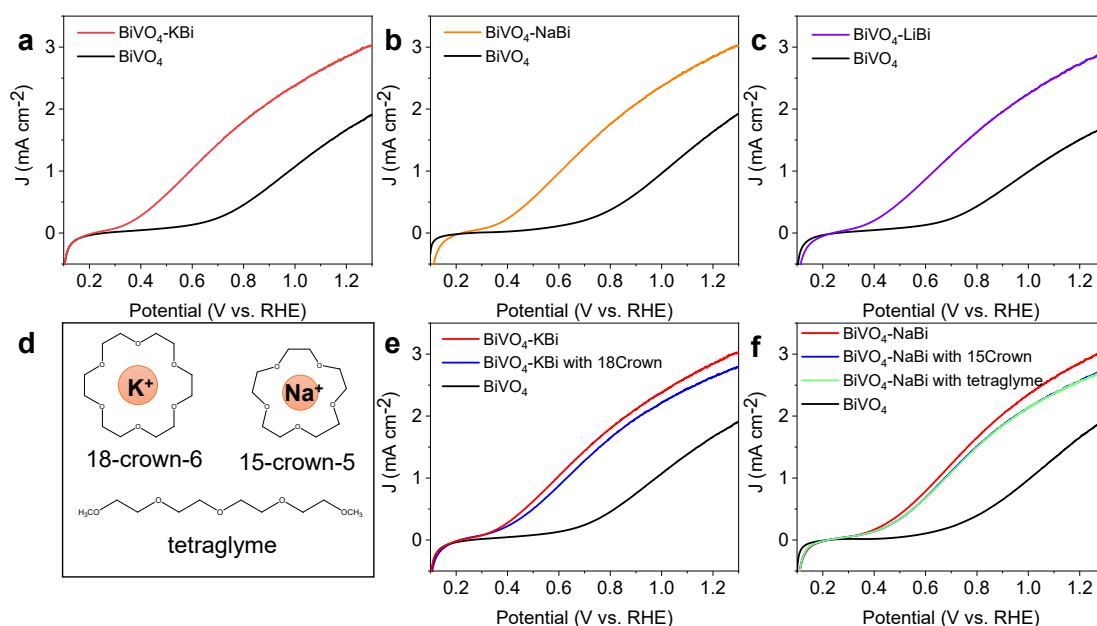
Figure S4. LSVs of BiVO4 photoanodes with treatment of soaking in (a) 0.5 M KBi pH 9.3, (b) 0.5 M NaBi pH 9.3 and (c) 0.5 M LiBi pH 9.3 buffers under LED illumination for 12 h (d) For chelating metal cations, the activation was conducted in (e) 0.5 M KBi buffer added with 0.5 M 18-Crown-6, (f) 0.5 M NaBi buffer added with 0.5 M 15-Crown-5 or tetraethylene glycol dimethyl ether (tetraglyme).

Considering the solubility of NaBi buffer under ambient temperature, we prepared 0.5 M pH 9.3 borate buffers with different alkali metal cations (Li^+, Na^+, K^+). The activated BiVO4 photoanodes in the three buffers with different metal cations have similar LSV activated curves (2.8 ~ 2.9 mA/cm^2 at 1.23 V_{RHE}). The slight difference is reasonable that metal cations can impact on the state of borate polyanion species and have possibly cation effect on water oxidation activity[7]. To further evaluate the influence of alkali metal cations, 18-Crown-6 and 15-Crown-5 were used to chelate K^+ and Na^+ cations, respectively[8]. Tetraethylene glycol dimethyl ether (tetraglyme) was added into NaBi buffer as a controlled experiment because of its similar molecular weight and functional groups to 15-Crown-5, while it cannot chelate Na^+ cations. With chelation of K^+ or Na^+ by crown ethers, the activated BiVO4 photoanodes still achieve pronounced enhancement of LSV performance with soaking treatment. The controlled sample with tetraglyme has almost the same LSV curve as the sample with 15-Crown-5, even though tetraglyme cannot chelate Na^+ cations.
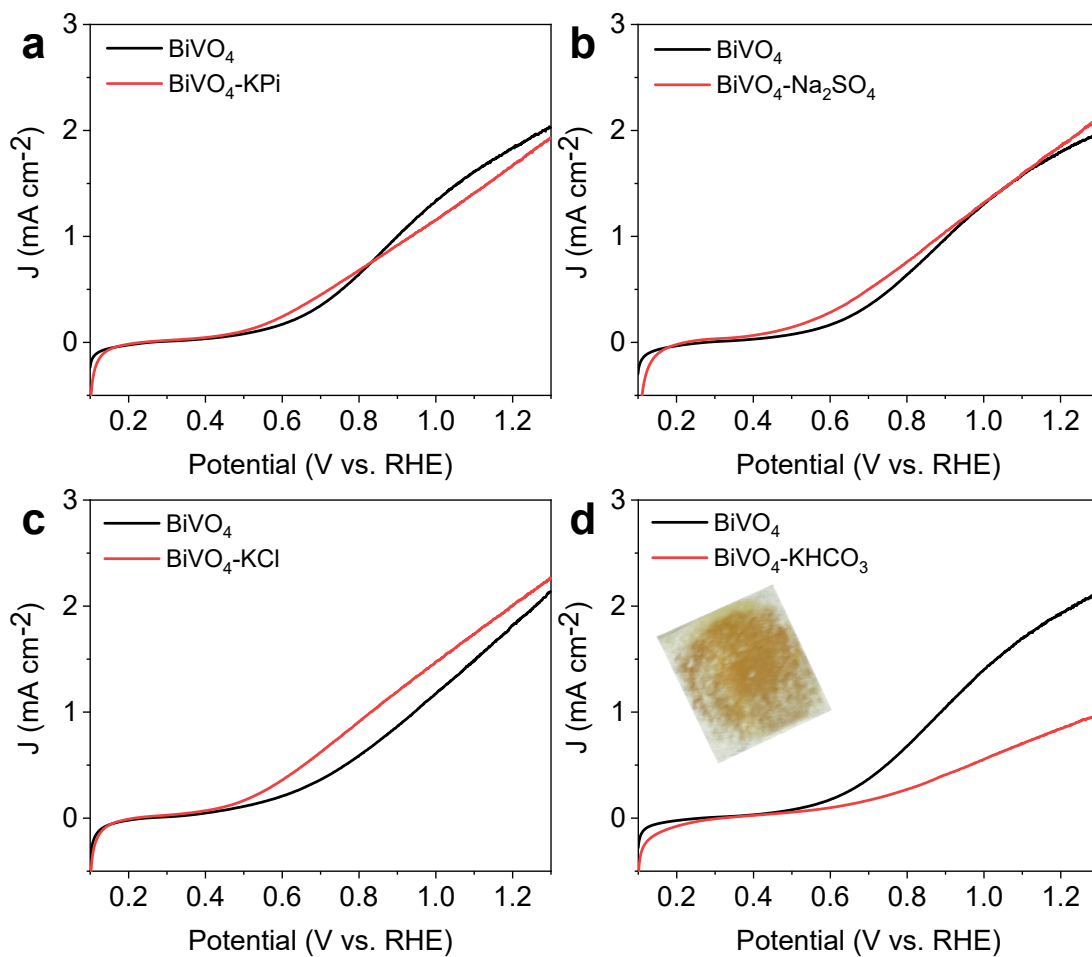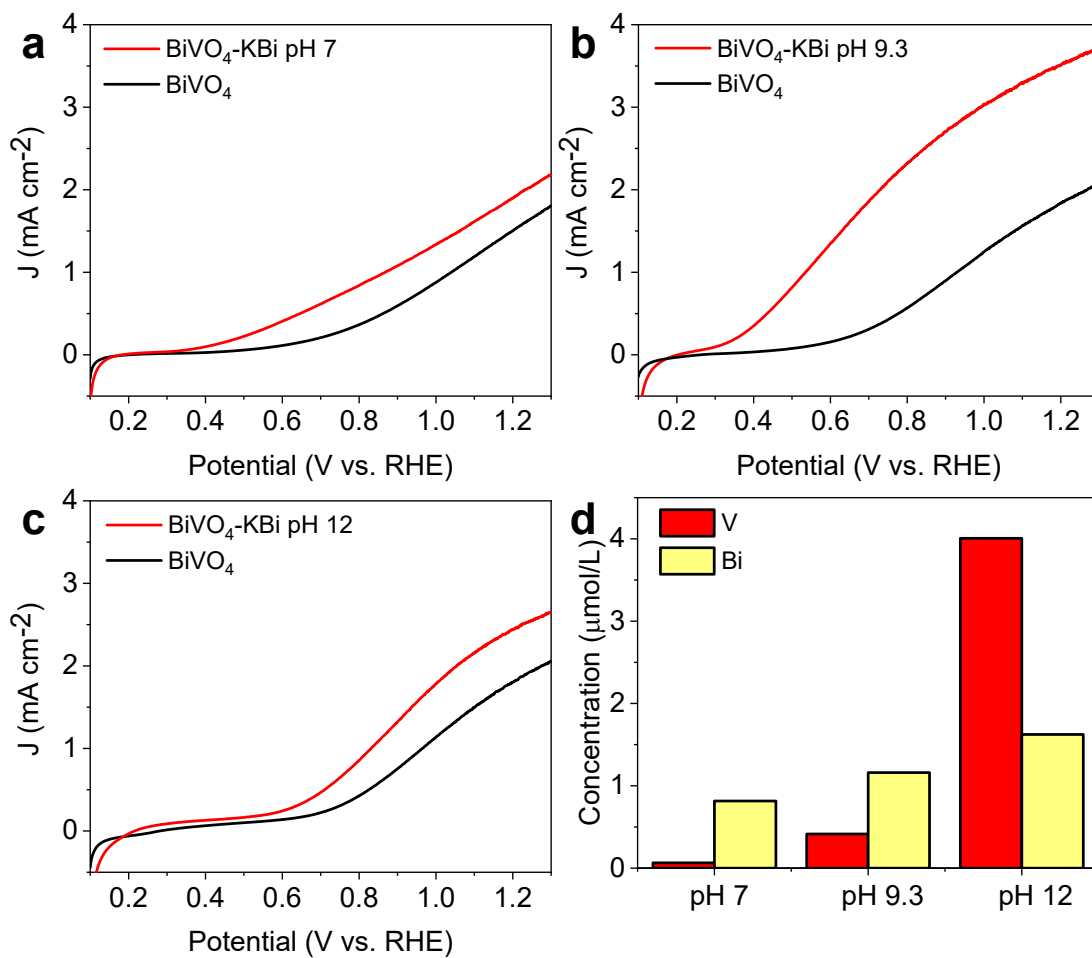
Figure S5. LSV curves of BiVO$_4$ photoanodes soaked in (a) 1 M KPi buffer (pH 9.3), (b) 1 M Na$_2$SO$_4$, (c) 1 M KCl, and (d) 1 M KHCO$_3$ (pH 8.4) solutions for 12 h under LED illumination. LSVs were all tested in 1 M KBi pH 9.3. The inset in (d) is photograph of BiVO$_4$ photoanodes after immersion in 1 M KHCO$_3$ solutions.
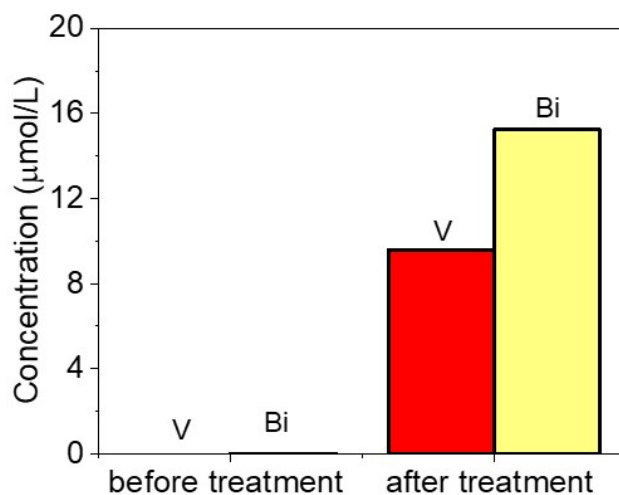
**Figure S6**. ICP of the 1 M KHCO$_3$ (pH 8.4) solution before and after soak treatment.

For bicarbonate solution particularly, the photocurrent density of BiVO$_4$ declines evidently after soak treatment. The inset in Figure S5d of BiVO$_4$ piece after soak treatment displays the broken BiVO$_4$ layer on fluorine doped tin oxide (FTO) glass, which results in photocurrent decay of BiVO$_4$ photoanode. The ICP results of bicarbonate solution after soak treatment prove that BiVO$_4$ material is corroded and dissolves significantly in bicarbonate soak treatment (Figure S6).

Figure S7. LSV curves of BiVO₄ photoanodes soaked in (a) 1 M KBi pH 7, (b) 1 M KBi pH 9.3, (c) 1 M KBi pH 12 solutions for 12 h under LED illumination. (d) ICP of the KBi buffer solutions after soak treatment.
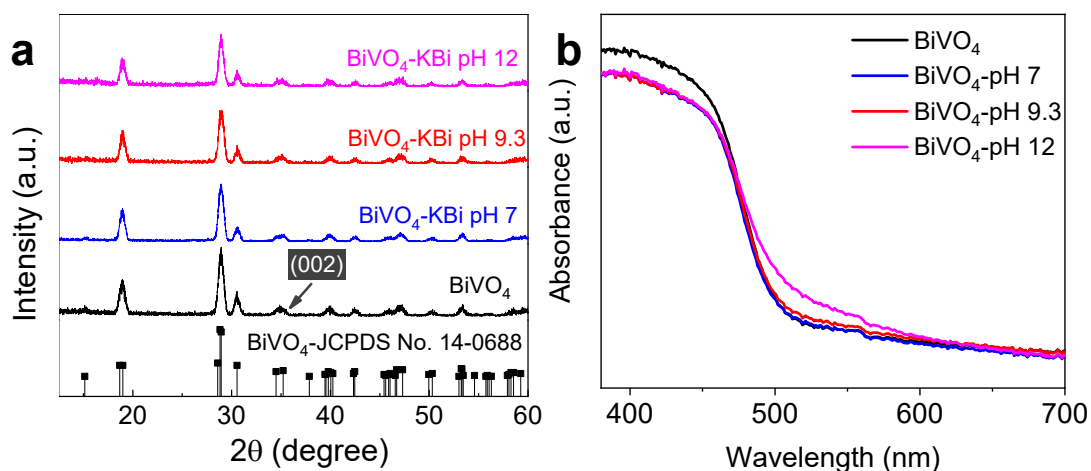
Figure S8. (a) XRD patterns of bare $BiVO_4$ and activated $BiVO_4$ in 1 M KBi pH 7, 1 M KBi pH 9.3, and 1 M KBi pH 12 at a small grazing angle (Omega = 0.5). (b) UV-vis spectra.
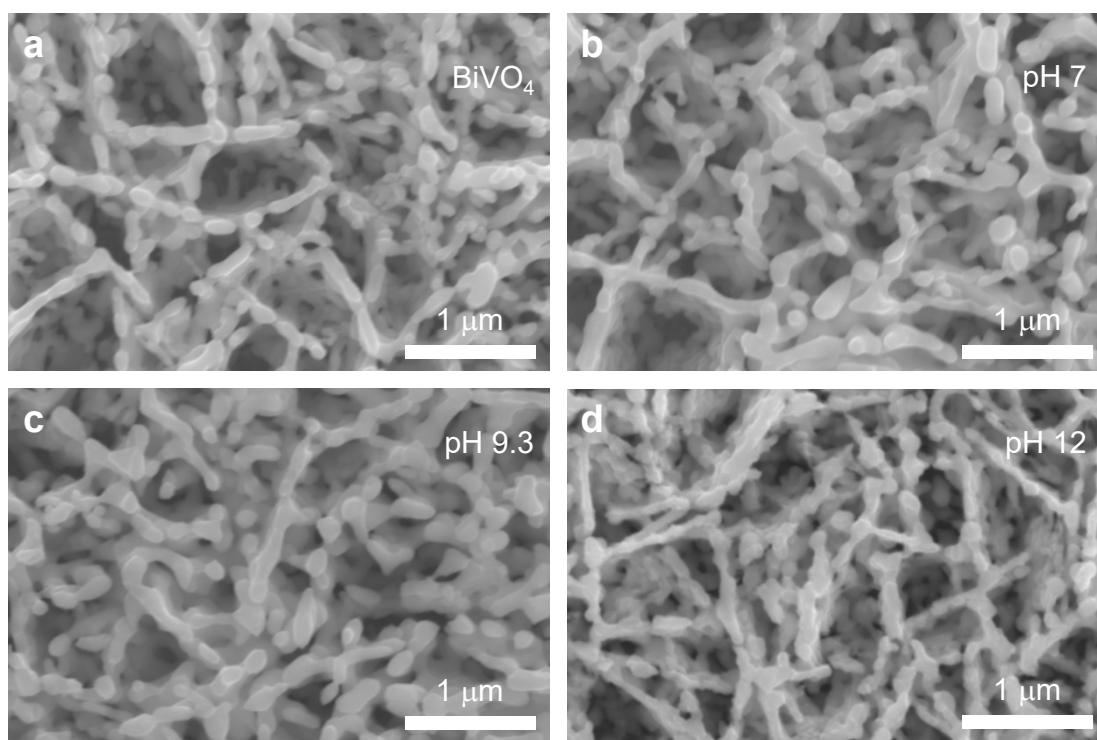
**Figure S9**. SEM images of (a) $BiVO_4$ and activated $BiVO_4$ photoanodes soaked in (b) 1 M KBi pH 7, (c) 1 M KBi pH 9.3, (d) 1 M KBi pH 12 buffers for 12 h under LED illumination.

The X-ray diffraction (XRD) peaks of $BiVO_4$ and activated $BiVO_4$ photoanodes can be well-matched with monoclinic $BiVO_4$ (Figure S8a). There are no new peaks, but the

peak intensity of activated $BiVO_4$ is slightly weakened. The UV-vis spectra shows no apparent change in bulk band absorbance after borate activation (Figure S8b). The small increases of absorbance around 520 nm along with increasing pH can be assigned to the defect-related features of activated $BiVO_4$ surface[9]. In addition, the SEM images indicate that the nanoporous structure of $BiVO_4$ is maintained across all samples, but the surfaces of the nanostructure become rougher as the pH increases (Figure S9). The process of vanadium dissolution can be described as the destruction of the surface of $BiVO_4$. From ICP results (Figure S7d), It clearly illustrates that the concentrations of vanadium dissolution into buffers increase with pH. Meanwhile, the concentration of dissolved Bi does not vary significantly across different pH values. This is because V tends to dissolve into aqueous solutions, particularly in more alkaline buffers[10, 11]. After the collapse of the $BiVO_4$ structure, Bi dissolves into buffers in a limited amount due to reoxidation and precipitation as BiO_x[12-14]. Understandably, excessive vanadium dissolution can undermine the activation performance, which explains why the photocurrent density of the pH 12 sample is lower than that of the pH 9.3 sample. However, the pH 7 sample, which loses the least amount of vanadium, has a smaller improvement in photocurrent than the pH 9.3 sample. This implies that there may be another reason, iron impurity.
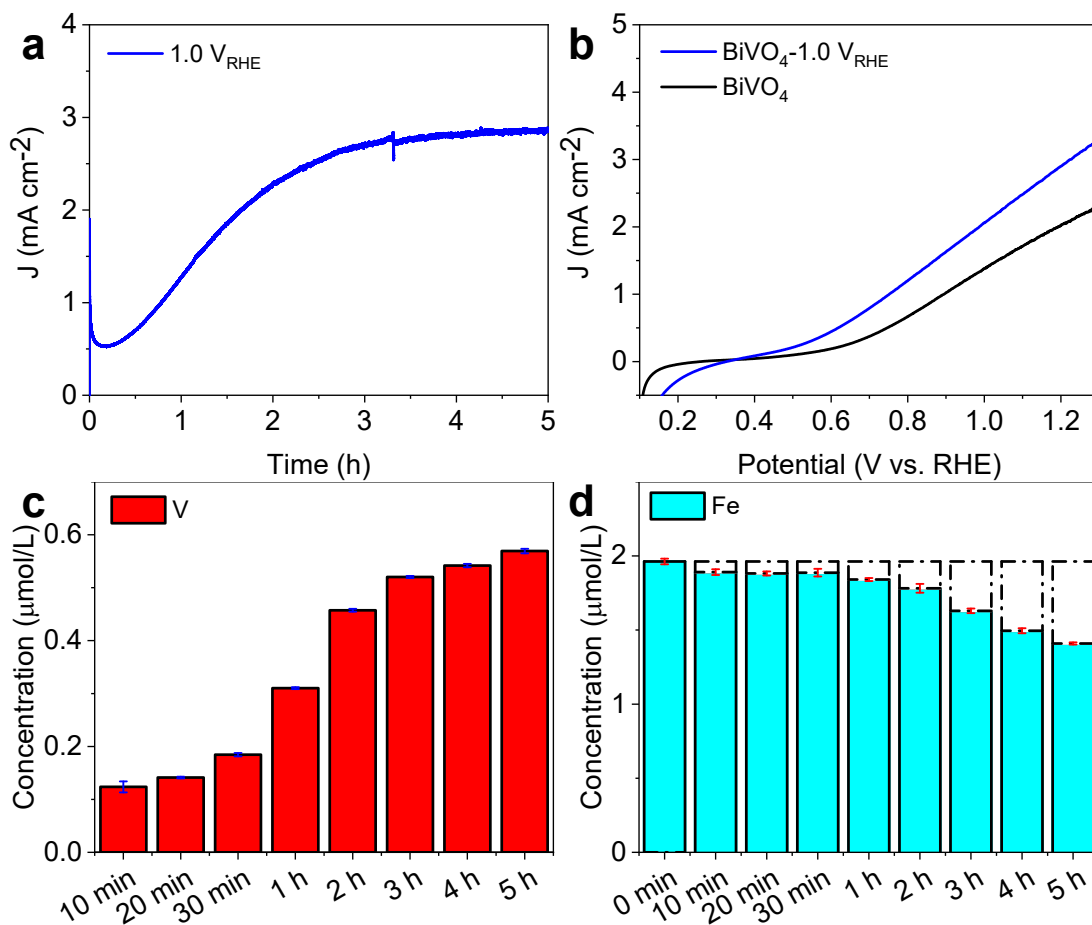
Figure S10. (a) J-t curve at 1.0 V vs. RHE of BiVO$_4$ photoanodes tested in 1 M KBi pH 9.3 under AM 1.5 G irradiation (100 mW/cm^2). (b) The LSV curves before and after J-t curve. ICP results of (c) V and (d) Fe in electrolyte used in J-t curve during different times.
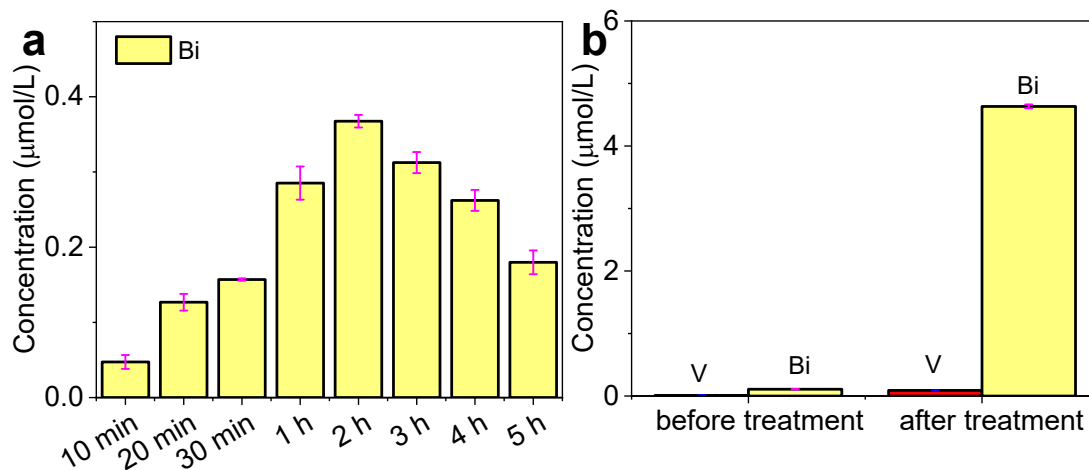
Figure S11. ICP results of (a) Bi in electrolyte used in J-t curve during different times (Figure S10a), (b) V and Bi detected on Pt counter electrode before and after photopolarization treatment. The Pt electrode was immersed in 2 M HNO_3 (4 mL) for preparing ICP samples.

The dissolved Bi also follows the increasing trend but starts to decrease after 2 h. The dissolved Bi will be reduced on Pt counter electrode.
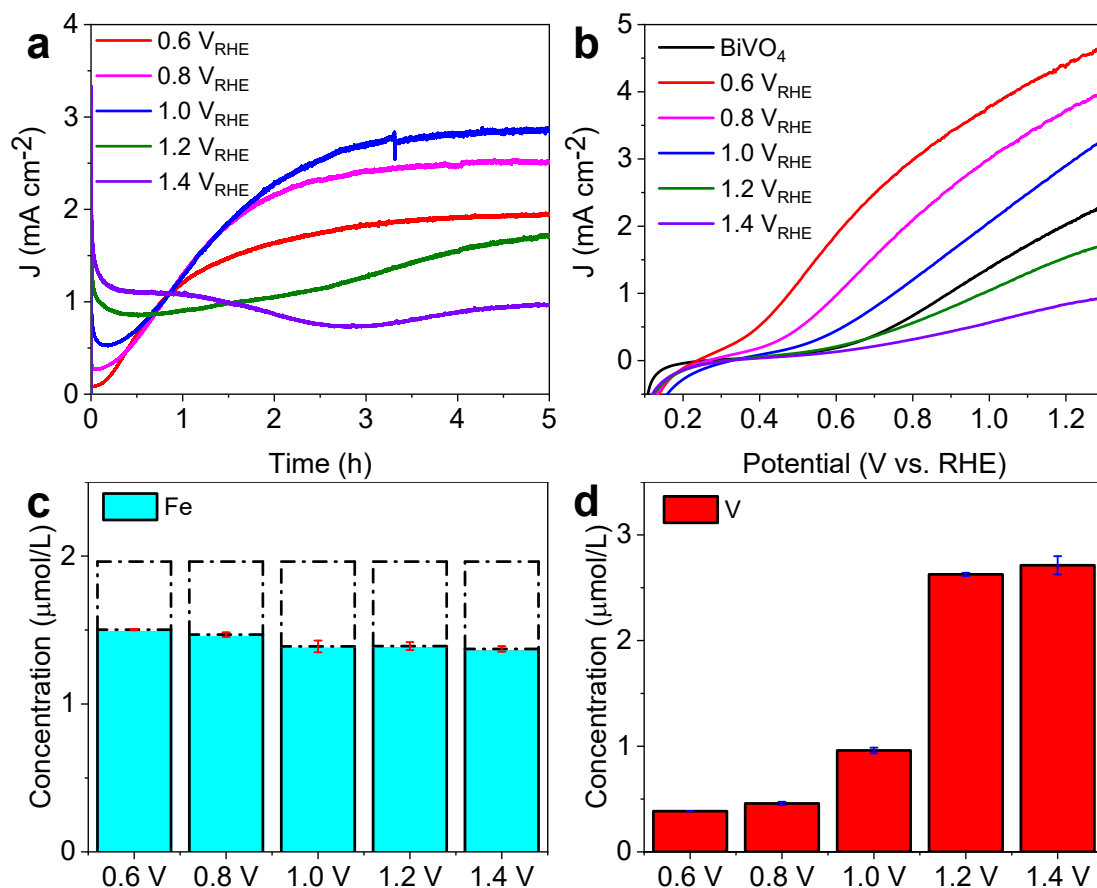
Figure S12. (a) i-t curves at different bias potentials of $BiVO_4$ photoanodes tested in 1 M KBi pH 9.3 for 5 hours and (b) their LSV curves before and after i-t. ICP of the remaining i-t electrolytes for (c) Fe and (d) V at 0.6 V_{RHE}, 0.8 V_{RHE}, 1.0 V_{RHE}, 1.2 V_{RHE}, and 1.4 V_{RHE} in 1 M KBi pH 9.3 buffer.

After borate activation with chronoamperometry under illumination, the first LSV curves were recorded for different bias potentials. The photocurrent densities at 1.23 V_{RHE} of activated $BiVO_4$ photoanodes follow the order of bias potential of 0.6 V_{RHE} > 0.8 V_{RHE} > 1.0 V_{RHE} > 1.2 V_{RHE} > 1.4 V_{RHE}. The photocurrent density of 0.6 V_{RHE} sample obtains 4.5 mA/cm^2 at 1.23 V_{RHE} as well as the best onset potential without any sacrificial agents.
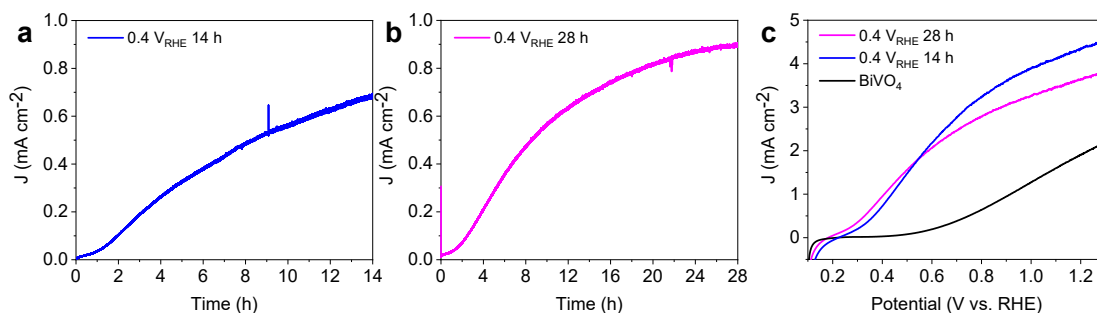
Figure S13. i-t curves at 0.4 V_{RHE} of $BiVO_4$ photoanodes tested in 1 M KBi pH 9.3 for (a) 14 hours and (b) 28 hours, and (c) its first LSV curves after i-t.

The photocurrent keeps rising over 14 hours (14-h) and reaches photocurrent plateau of 0.9 mA/cm^2 around 28 hours (28-h). The first LSV curves recorded after i-t at 0.4 V_{RHE} reveal the satisfactory activation results. At 1.23 V_{RHE}, the activated $BiVO_4$ photoanodes obtains 4.4 mA/cm^2 and 3.7 mA/cm^2 for 14-h and 28-h samples respectively, which is close to the photocurrent density at 0.6 V_{RHE} activation (4.5 mA/cm^2). The 28-h sample has more negative onset potential (~0.2 V) than 14-h sample. However, its photocurrent density is lower even though its activation plateau (0.9 mA/cm^2) is higher than that of 14-h sample (0.7 mA/cm^2). This can be attributed to the loss and reoxidation of surface active site due to the long working time and generated oxygen.
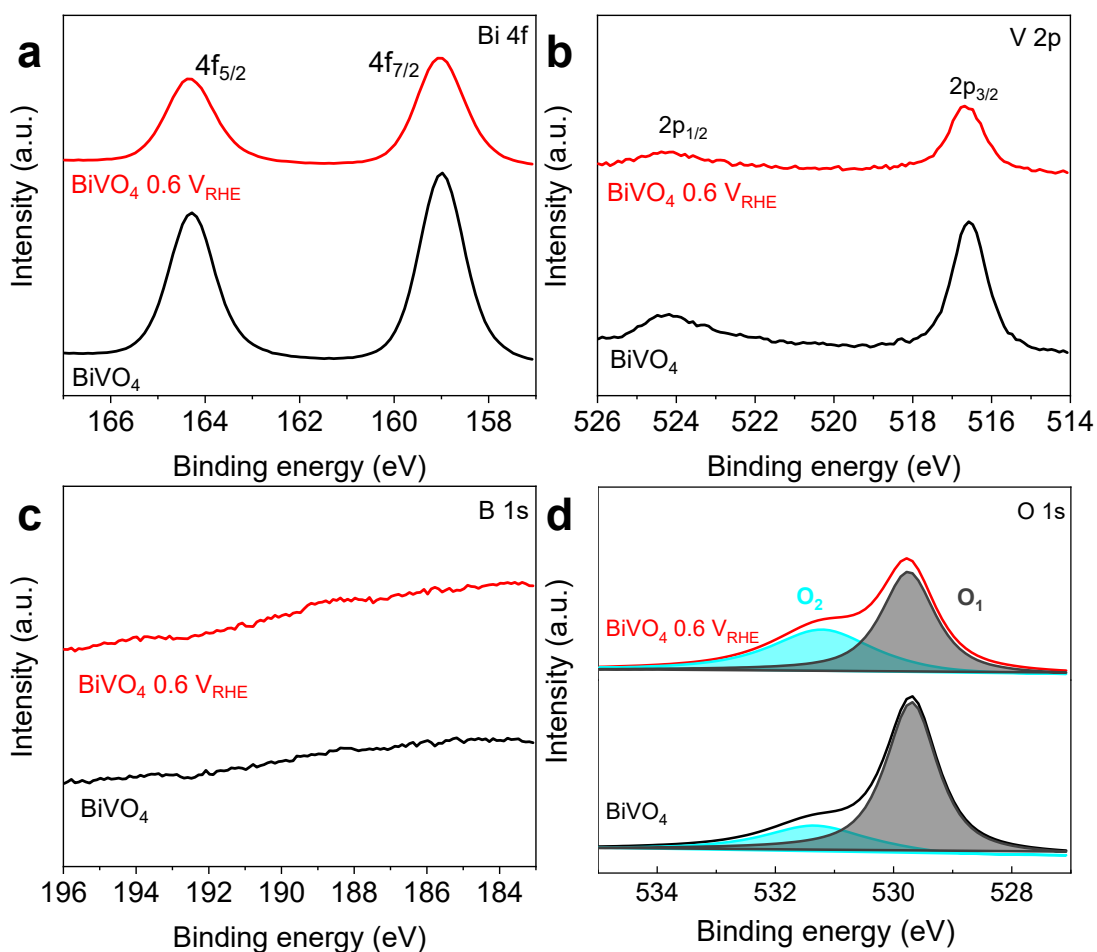
Figure S14. (a) Bi 4f, (b) V 2p, (c) B 1s, and (d) O 1s XPS spectra of $BiVO_4$ before and after activation.

The O 1s spectra were also examined and deconvoluted into two peaks. For the deconvoluted peaks, the O_1 peak representing metal oxide becomes weaker and O_2 peak is stronger. The more prominent O_2 peak is commonly associated with hydroxyl species, adsorbed molecular water and/or oxygen vacancy[6, 15, 16].

Table S1 atomic ratio of surface elemental composition (%) from XPS spectra

| element	$BiVO_4$ 0.6 V_{RHE}	$BiVO_4$
Bi 4f	6.58	8.98
V 2p	3.24	4.93
Fe 2p	3.79	0.78
V/Bi	**0.15**	**0.54**
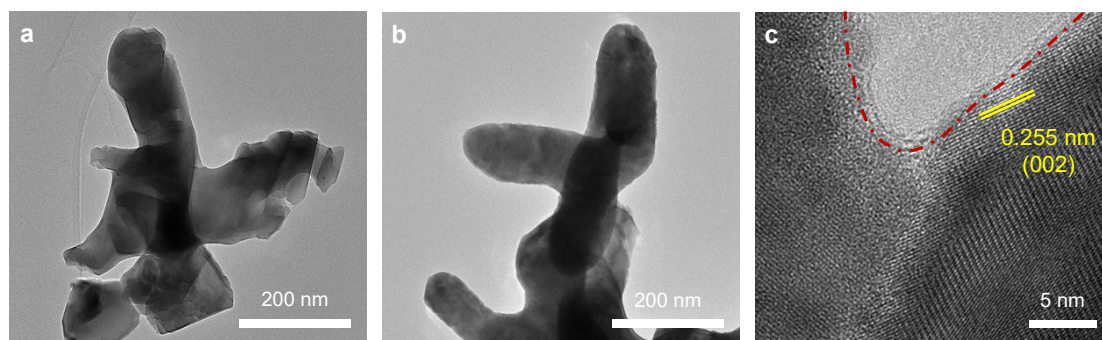
Figure S15. TEM images of (a) BiVO$_4$ and (b) activated BiVO$_4$ photoanodes, and (c) HRTEM images of activated BiVO$_4$ photoanode.

In Figure S15c, the lattice fringes corresponding to the (002) intralayer spacing of 0.255 nm were detected in the bulk region of BiVO$_4$. This crystal plane is shown at 35.221 of 2θ degrees in the XRD data (Figure S8).

Table S2 atomic fraction (%) of elemental composition from TEM-EDS

element	family	atomic fraction
O	K	60.09
V	K	20.25
Fe	K	0.59
Bi	L	19.07
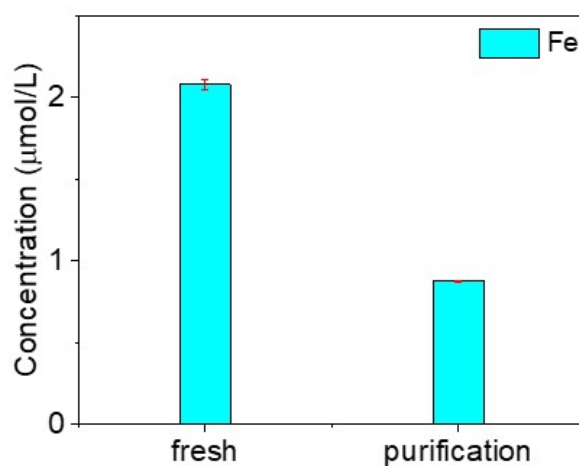
Figure S16. ICP results of Fe in KBi buffer before and after electrolyte purification.
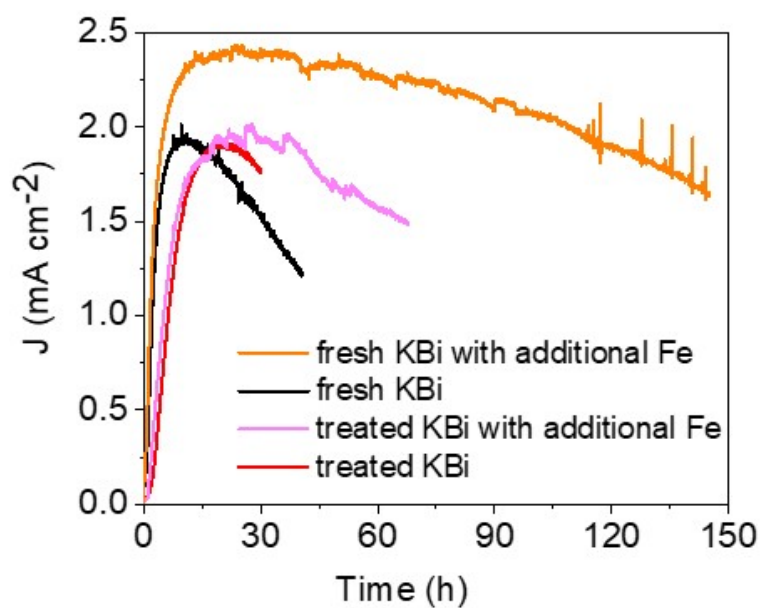
Figure S17. J-t curves of $BiVO_4$ photoanode tested at 0.6 V_{RHE} in KBi buffer with/without purification treatment.
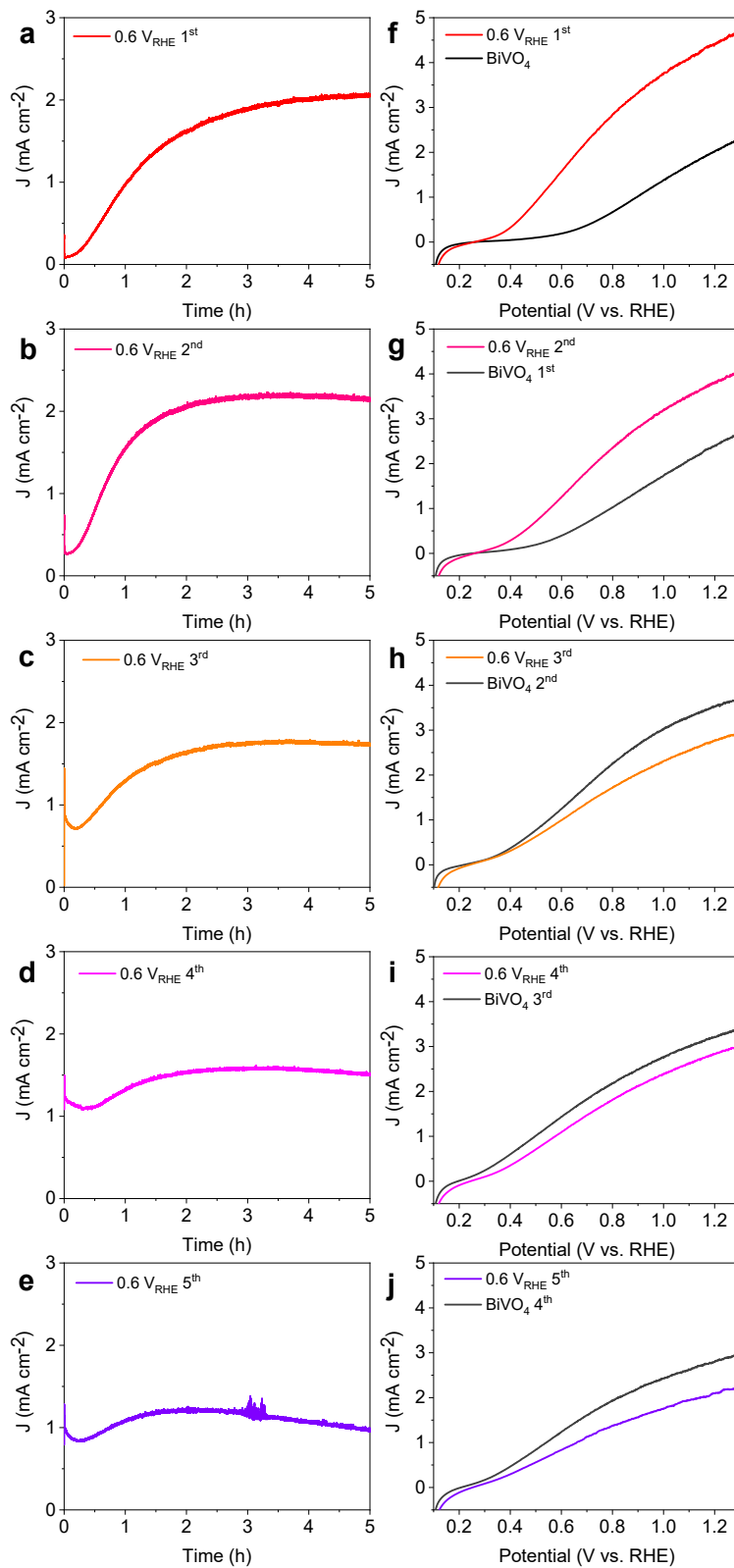
Figure S18. i-t curves of $BiVO_4$ photoanode tested at 0.6 V_{RHE} in 1 M KBi pH 9.3 for 5 hours under illumination (a-e), and corresponding LSV curves before and after i-t (f-j). The piece of electrode was dried naturally before each test.
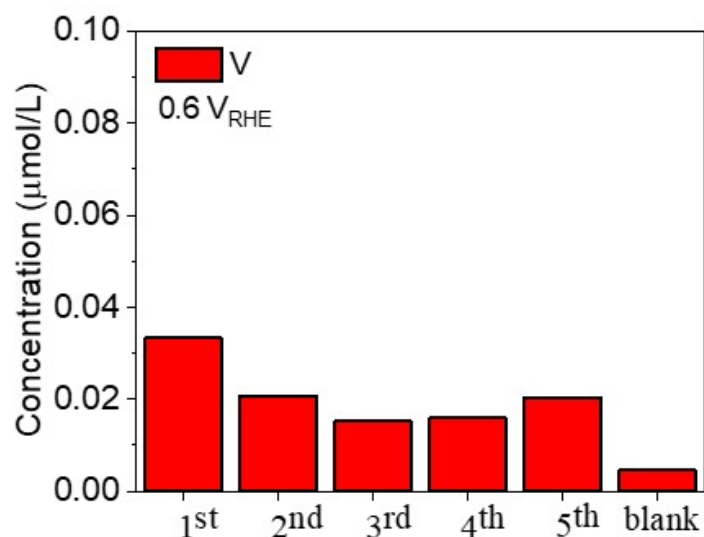
Figure S19. ICP of the remaining i-t electrolytes of **Figure S20a-e**.

From Figure S18, the first potentiostatic activation gradually reaches a photocurrent plateau around 2.1 mA/cm^2, and the photocurrent density of the LSV curve after activation achieves ~4.5 mA/cm^2 at 1.23 V$_{RHE}$. However, the apparent decreasing of plateau photocurrent can be observed for cycle tests from ~ 2.1 mA/cm^2 to ~ 1.0 mA/cm^2. Their LSV curves after J-t tests become poorer as cycle tests replacing with new electrolyte each time. ICP results of vanadium in the each remaining J-t electrolyte help to explain the descending performance of this piece of BiVO$_4$ electrode within succession borate activation. The ICP values of 2nd-5th J-t tests are still located around 0.015-0.02 μmol/L in spite of 0.03 μmol/L for the value of 1st J-t test. For the J-t curves, the photocurrent plateau means that vanadium dissolution is mostly suppressed discussed above. However, according to the PEC performance and ICP results, it indicates the surface vanadium will continually dissolve into electrolytes regardless of the formation of a certain Fe activated layer. In this work, a V^{5+}-saturated electrolyte was prepared for long-term stability test according to Choi's work[17]. On the basis of Figure S20, BiVO$_4$ can still be activated by borate buffer though that takes more time to a photocurrent plateau. More importantly, after creating V^{5+}-saturated condition, the long-term stability is apparently improved, which originates from the inhibition of continuous vanadium dissolution. The protection strategy of V^{5+}-saturated electrolyte

makes borate activation by iron impurities more meaningful.
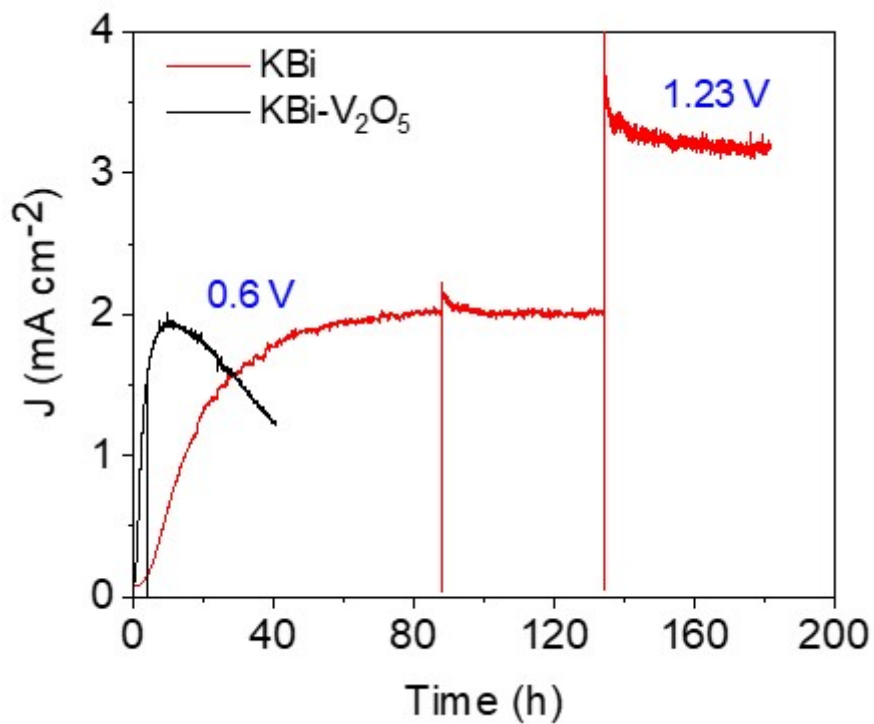
Figure S20. J-t curves of $BiVO_4$ photoanode tested at 0.6 V_{RHE} in 1 M KBi pH 9.3 with or without 50 mM V_2O_5 under illumination
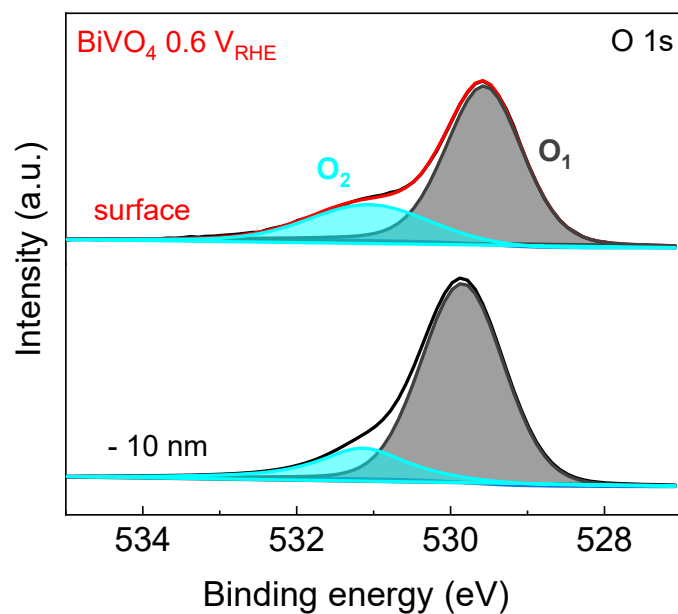
Figure S21. O 1s XPS spectra of $BiVO_4$ and activated $BiVO_4$ photoanodes with etching 10 nm by Ar^+ sputtering.

It shows the difference for activated $BiVO_4$ after an etching treatment by Ar^+ sputtering. After etching treatment, the bulk $BiVO_4$ mainly exposes O_1 peak standing for metal oxide. It suggests that the $BiVO_4$ surface emerges a substantial change of its composition with the formation of Fe activated layer.
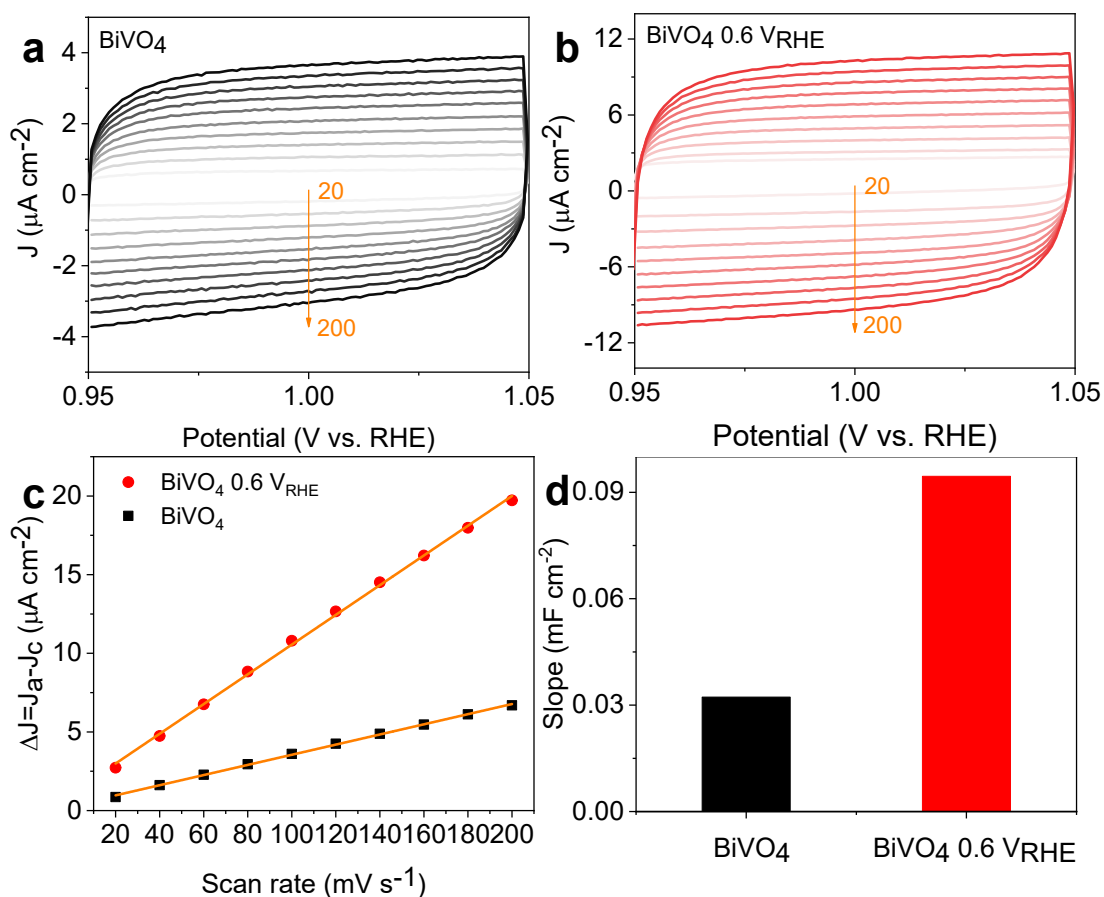
Figure S22. Cyclic voltammetry for (a) bare $BiVO_4$ and (b) activated $BiVO_4$ photoanodes at different scan rates (mV/s). (c) Charging current density differences plotted against scan rates and (d) their fitted slopes.

The electrochemical active surface area of photoanodes can be compared by the characteristic of double-layer capacitance, because the photoanodes have similar nanostructures avoiding much interference with results. The capacitive currents were obtained at different scan-rate by cyclic voltammetry (20, 40, 60, 80, 100, 120, 140, 160, 180 and 200 mV/s). The double-layer capacitance was estimated by plotting the $\Delta J=(J_a-J_c)$ against the scan rate, which J_a and J_c were read at 1.0 V vs. RHE. The linear slope is fixed proportionally to the capacitance, which can be used to represent the electrochemical active surface area of photoanode[18, 19].

Table S3 Detailed comparison of the ABPE and photocurrent of $BiVO_4$ photoanodes without extra cocatalysts

Method	ABPE	J at 1.23 V_{RHE}	Reference
This work (0.6 V_{RHE})	**1.2 % (0.76 V_{RHE})**	**4.5 mA/cm^2**	This work
This work (0.4 V_{RHE})	**1.5 % (0.7 V_{RHE})**	**4.4 mA/cm^2**	This work
soaking (buffer)	1.1 % (~ 0.7 V_{RHE})	3.5 mA/cm^2	[20]
electrochemistry (O_V)	~ 0.6 % (~ 0.84 V_{RHE})	2.5 mA/cm^2	[21]
immersion (Na_2SO_3)	0.27 % (1.0 V_{RHE})	2.2 mA/cm^2	[22]
O_v formation	0.24 % (-)	1.75 mA/cm^2	[23]
photoetching (O_v)	-	~2.0 mA/cm^2	[24]
photopolarization	-	4.6 mA/cm^2	[6]
photocharging	-	4.3 mA/cm^2	[5]
photoetching (BiO_x)	0.85 % (0.75 V_{RHE})	3.2 mA/cm^2	[14]
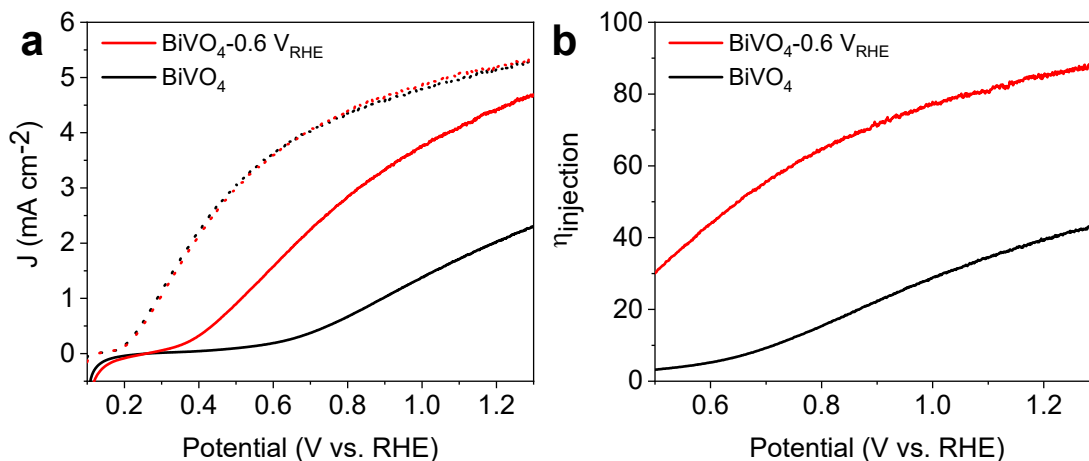
Figure S23. (a) LSV curves of $BiVO_4$ and activated $BiVO_4$ photoanodes tested in 1 M KBi pH 9.3 without (solid line) or with 0.2 M Na_2SO_3 (dash line) under illumination. (b) Charge injection efficiency calculated from LSV results.

The photoelectrode efficiencies normally involve light absorption efficiency ($\eta_{absorption}$), charge separation efficiency ($\eta_{separation}$), and charge injection efficiency ($\eta_{injection}$). The $\eta_{absorption}$ almost remains the same before and after borate activation because of photoelectrodes without any cocatalysts and the trivial change of light absorption (Figure S8b). For $\eta_{separation}$, it represents the charge separation capability in $BiVO_4$ bulk. Here, with 0.2 M $NaSO_3$ as a hole scavenger, it is assumed that holes arriving $BiVO_4$ surface can be completely consumed by oxidation reaction.
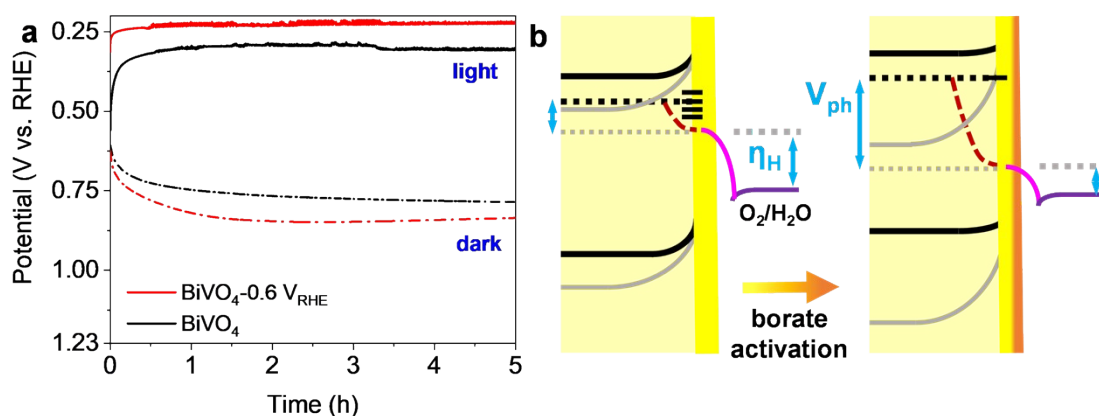
Figure S24. (a) The open circuit potential tests of bare $BiVO_4$ and activated $BiVO_4$ photoanodes with and without illumination. (b) Band diagrams under open-circuit condition before and after borate activation. Band diagram under illumination is shown in black line and band diagram under dark is shown in gray line.

OCP results with and without illumination record the potentials with a zero net exchange current across the electrode/electrolyte interface. Without illumination under dark condition, the ideal OCP value as Fermi level (electrons) should have been balanced with the redox reaction potential in the electrolyte. With illumination, the OCP value as quasi-Fermi level of holes generally implies the onset potential of LSV curves. However, because of severe surface states, a considerable potential drop occurs within the Helmholtz layer (η_H), which negatively impacts on photoanode's photovoltage (V_{ph})[25]. It is reasonable that severe surface states often play the role of recombination centers for photo-generated carriers and intensify the kinetic overpotential of surface reaction[26, 27]. The V_{ph} of bare $BiVO_4$ photoanode is unreasonably low, which value is assumed around 0.2 V considering the constant activation process regardless of external environment. During the OCP experiment for bare $BiVO_4$, the borate activation continuously ameliorates V_{ph} value within 5 hours. It actually means that activated surface layer formed in-situ with borate activation has fewer surface states than bare $BiVO_4$. And for activated $BiVO_4$, its initial V_{ph} value is about 0.4 V due to some regenerated surface states when the photoanode is removed from activation equilibrium

and exposed to air[12, 20]. Furthermore, the V_{ph} value for activated $BiVO_4$ photoanode achieves Ca. 0.6 V within 5 hours for OCP experiment. Based on the OCP results and discussion above, the band diagrams under open-circuit condition before and after borate activation is illustrated in Figure S24b.
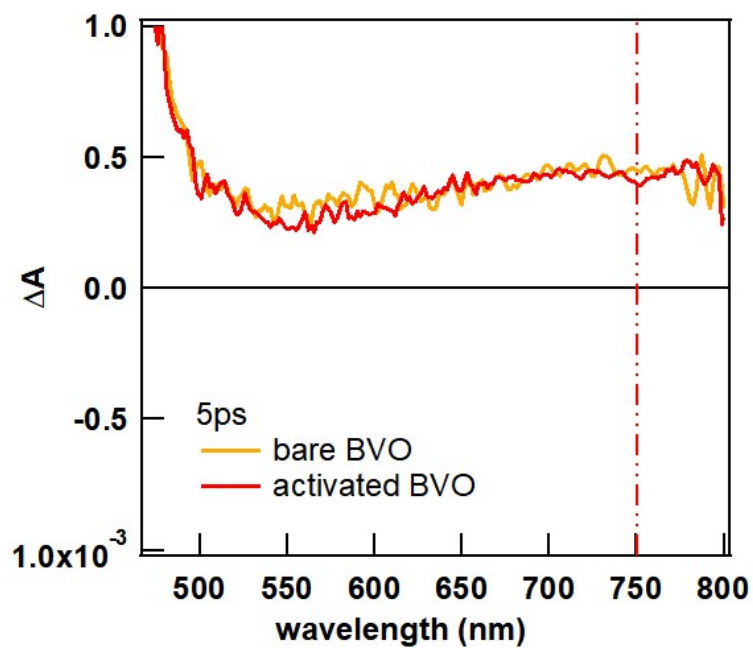
Figure S25. Transient absorption spectra of bare BiVO$_4$ (BVO) and activated BiVO$_4$.
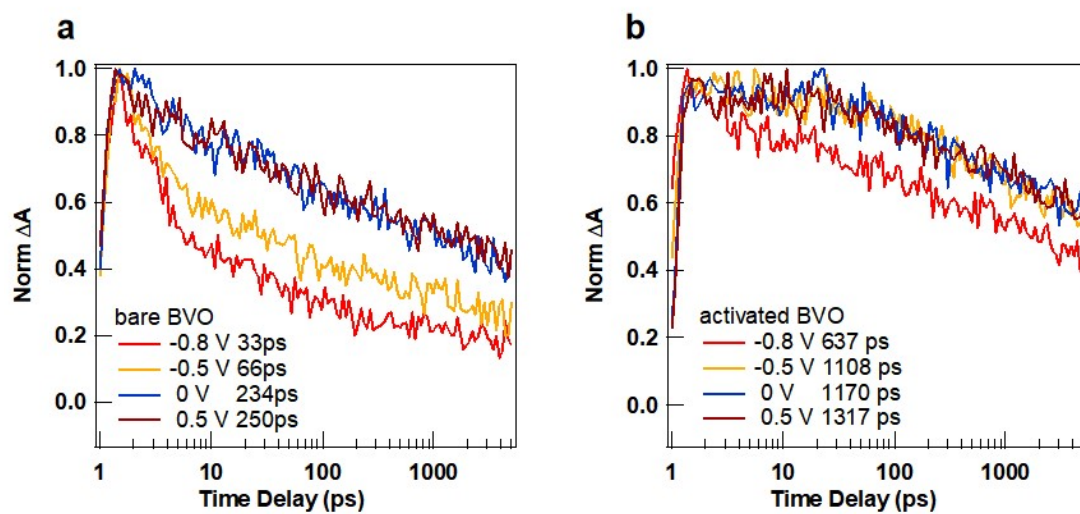
Figure S26. Carrier dynamics of (a) bare BiVO$_4$ (BVO) and (b) activated BiVO$_4$ at different bias potentials (V vs. Ag/AgCl, 3.5 M KCl).
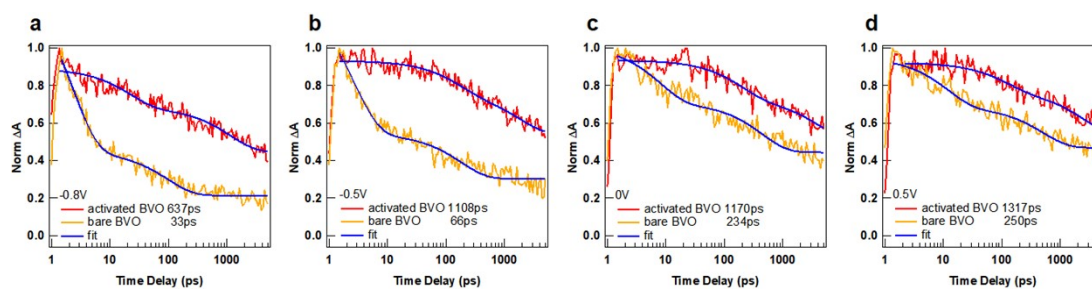
Figure S27. Carrier dynamics of bare $BiVO_4$ (BVO) and activated $BiVO_4$ at (a) -0.8 $V_{Ag/AgCl}$, (b) -0.5 $V_{Ag/AgCl}$, (c) 0 $V_{Ag/AgCl}$ and (d) 0.5 $V_{Ag/AgCl}$ ($V_{RHE} = V_{Ag/AgCl} + \sim 0.8$).

Utilizing a pump light source at 3.1 eV and applying a bias potential of 0 V versus Ag/AgCl, the transient absorption spectra for the bare and activated $BiVO_4$ samples at 5 ps are presented in Figure S25. Positive signals were detected in the wavelength range from 480 nm to 800 nm. A prominent feature at 750 nm, which exhibited a favorable signal-to-noise ratio and comprehensible dynamics, was selected for kinetic analysis. In order to explore the impact of the Fe activated layer on carrier behavior, a comparative study was conducted on the carrier dynamics of bare $BiVO_4$ and activated $BiVO_4$ under different bias potentials. Figure S26 illustrates the carrier lifetime obtained by fitting with a dynamic model, which exhibits a negative correlation with the carrier recombination strength. As the applied bias potential increases from -0.8 $V_{Ag/AgCl}$ to 0.5 $V_{Ag/AgCl}$, a slower rate of carrier recombination was observed. Figure S26a shows that the carrier lifetime of bare $BiVO_4$ increased from 33 ps to 250 ps, while Figure S26b shows that the carrier lifetime of activated $BiVO_4$ increased from 637 ps to 1317 ps. It is speculated that with the increase of applied bias potential, the Fermi level of $BiVO_4$ moves downwards, increasing the transfer of holes to the solution, which blocks the recombination of electrons and results in an extended carrier lifetime. Figure S27 compares the carrier dynamics of bare $BiVO_4$ and activated $BiVO_4$ under different applied bias potentials. Activated $BiVO_4$ displays a slower rate of carrier recombination attributed to its longer carrier lifetime, which is consistent with the higher photocurrent observed in the LSV curves.

References

1. Kim, T. W.; Choi, K.-S., Nanoporous BiVO$_4$ Photoanodes with Dual-Layer Oxygen Evolution Catalysts for Solar Water Splitting. *Science* **2014,** *343*, 990-994.

2. Zheng, M.; Cao, X.; Ding, Y.; Tian, T.; Lin, J., Boosting photocatalytic water oxidation achieved by BiVO$_4$ coupled with iron-containing polyoxometalate: Analysis the true catalyst. *J. Catal.* **2018,** *363*, 109-116.

3. Xiao, M.; Luo, B.; Wang, Z.; Wang, S.; Wang, L., Recent Advances of Metal‐Oxide Photoanodes: Engineering of Charge Separation and Transportation toward Efficient Solar Water Splitting. *Solar RRL* **2020,** *4* (8).

4. Wu, Y.; Jiang, Z.; Lu, X.; Liang, Y.; Wang, H., Domino electroreduction of CO$_2$ to methanol on a molecular catalyst. *Nature* **2019,** *575* (7784), 639-642.

5. Trześniewski, B. J.; Digdaya, I. A.; Nagaki, T.; Ravishankar, S.; Herraiz-Cardona, I.; Vermaas, D. A.; Longo, A.; Gimenez, S.; Smith, W. A., Near-complete suppression of surface losses and total internal quantum efficiency in BiVO$_4$ photoanodes. *Energy Environ. Sci.* **2017,** *10* (6), 1517-1529.

6. Gao, R. T.; Wang, L., Stable Cocatalyst-Free BiVO$_4$ Photoanodes with Passivated Surface States for Photocorrosion Inhibition. *Angew. Chem. Int. Ed.* **2020,** *59* (51), 23094-23099.

7. Ding, C.; Zhou, X.; Shi, J.; Yan, P.; Wang, Z.; Liu, G.; Li, C., Abnormal effects of cations (Li$^+$, Na$^+$, and K$^+$) on photoelectrochemical and electrocatalytic water splitting. *The journal of physical chemistry. B* **2015,** *119* (8), 3560-6.

8. Malkani, A. S.; Li, J.; Oliveira, N. J.; He, M.; Chang, X.; Xu, B.; Lu, Q., Understanding the electric and nonelectric field components of the cation effect on the electrochemical CO reduction reaction. *Sci Adv* **2020,** *6* (45).

9. Firet, N. J.; Venugopal, A.; Blommaert, M. A.; Cavallari, C.; Sahle, C. J.; Longo, A.; Smith, W. A., Chemisorption of Anionic Species from the Electrolyte Alters the Surface Electronic Structure and Composition of Photocharged BiVO$_4$. *Chem. Mater.* **2019,** *31* (18), 7453-7462.

10. Toma, F. M.; Cooper, J. K.; Kunzelmann, V.; McDowell, M. T.; Yu, J.;

Larson, D. M.; Borys, N. J.; Abelyan, C.; Beeman, J. W.; Yu, K. M.; Yang, J.; Chen, L.; Shaner, M. R.; Spurgeon, J.; Houle, F. A.; Persson, K. A.; Sharp, I. D., Mechanistic insights into chemical and photochemical transformations of bismuth vanadate photoanodes. *Nature communications* **2016,** *7*, 12012.

11. Povar, I.; Spinu, O.; Zinicovscaia, I.; Pintilie, B.; Ubaldini, S., Revised Pourbaix diagrams for the vanadium-water system. *J. Electrochem. Sci. Eng.* **2019,** *9* (2), 75-84.

12. Nakajima, T.; Miseki, Y.; Tateno, H.; Tsuchiya, T.; Sayama, K., Acid-Resistant $BiVO_4$ Photoanodes: Insolubility Control by Solvents and Weak W Diffusion in the Lattice. *ACS Appl. Mater. Interfaces* **2021,** *13* (10), 12079-12090.

13. Zhang, S.; Rohloff, M.; Kasian, O.; Mingers, A. M.; Mayrhofer, K. J. J.; Fischer, A.; Scheu, C.; Cherevko, S., Dissolution of $BiVO_4$ Photoanodes Revealed by Time-Resolved Measurements under Photoelectrochemical Conditions. *J. Phys. Chem. C* **2019,** *123* (38), 23410-23418.

14. Chen, X.; Zhen, C.; Li, N.; Jia, N.; Xu, X.; Wang, L.; Liu, G., Photochemically Etching $BiVO_4$ to Construct Asymmetric Heterojunction of $BiVO_4/BiO_X$ Showing Efficient Photoelectrochemical Water Splitting. *Small Methods* **2023,** *7* (3), e2201611.

15. Qiu, W.; Xiao, S.; Ke, J.; Wang, Z.; Tang, S.; Zhang, K.; Qian, W.; Huang, Y.; Huang, D.; Tong, Y.; Yang, S., Freeing the Polarons to Facilitate Charge Transport in $BiVO_4$ from Oxygen Vacancies with an Oxidative 2D Precursor. *Angew. Chem. Int. Ed.* **2019,** *58* (52), 19087-19095.

16. Zhang, B.; Wang, L.; Zhang, Y.; Ding, Y.; Bi, Y., Ultrathin FeOOH Nanolayers with Rich Oxygen Vacancies on $BiVO_4$ Photoanodes for Efficient Water Oxidation. *Angew. Chem. Int. Ed.* **2018,** *57*, 2248-2252.

17. Lee, D. K.; Choi, K.-S., Enhancing long-term photostability of $BiVO_4$ photoanodes for solar water splitting by tuning electrolyte composition. *Nat. Energy* **2018,** *3* (1), 53-60.

18. Merki, D.; Vrubel, H.; Rovelli, L.; Fierro, S.; Hu, X., Fe, Co, and Ni ions promote the catalytic activity of amorphous molybdenum sulfide films for hydrogen

evolution. *Chem. Sci.* **2012,** *3* (8), 2515-2525.

19. Song, F.; Hu, X., Ultrathin cobalt-manganese layered double hydroxide is an efficient oxygen evolution catalyst. *J. Am. Chem. Soc.* **2014,** *136* (47), 16481-16484.

20. Meng, Q.; Zhang, B.; Fan, L.; Liu, H.; Valvo, M.; Edstrom, K.; Cuartero, M.; de Marco, R.; Crespo, G. A.; Sun, L., Efficient $BiVO_4$ Photoanodes by Postsynthetic Treatment: Remarkable Improvements in Photoelectrochemical Performance from Facile Borate Modification. *Angew. Chem. Int. Ed.* **2019,** *58* (52), 19027-19033.

21. Wang, S.; Chen, P.; Yun, J. H.; Hu, Y.; Wang, L., An Electrochemically Treated $BiVO_4$ Photoanode for Efficient Photoelectrochemical Water Splitting. *Angew. Chem. Int. Ed.* **2017,** *56* (29), 8500-8504.

22. Peng, Y.; Wu, H.; Yuan, M.; Li, F.-F.; Zou, X.; Ng, Y. H.; Hsu, H.-Y., Chemical reduction-induced surface oxygen vacancies of $BiVO_4$ photoanodes with enhanced photoelectrochemical performance. *Sustain. Energy Fuels* **2021,** *5* (8), 2284-2293.

23. Wang, S.; He, T.; Chen, P.; Du, A.; Ostrikov, K. K.; Huang, W.; Wang, L., In Situ Formation of Oxygen Vacancies Achieving Near-Complete Charge Separation in Planar $BiVO_4$ Photoanodes. *Advanced materials* **2020,** *32* (26), e2001385.

24. Feng, S.; Wang, T.; Liu, B.; Hu, C.; Li, L.; Zhao, Z. J.; Gong, J., Enriched Surface Oxygen Vacancies of Photoanodes by Photoetching with Enhanced Charge Separation. *Angew. Chem. Int. Ed.* **2020,** *59* (5), 2044-2048.

25. Du, C.; Yang, X.; Mayer, M. T.; Hoyt, H.; Xie, J.; McMahon, G.; Bischoping, G.; Wang, D., Hematite-based water splitting with low turn-on voltages. *Angew. Chem. Int. Ed.* **2013,** *52* (48), 12692-12695.

26. Shi, Q.; Murcia-López, S.; Tang, P.; Flox, C.; Morante, J. R.; Bian, Z.; Wang, H.; Andreu, T., Role of Tungsten Doping on the Surface States in $BiVO_4$ Photoanodes for Water Oxidation: Tuning the Electron Trapping Process. *ACS Catal.* **2018,** *8* (4), 3331-3342.

27. Kaneko, H.; Minegishi, T.; Domen, K., Recent Progress in the Surface

Modification of Photoelectrodes toward Efficient and Stable Overall Water Splitting. *Chemistry* **2018,** *24* (22), 5697-5706.